

# Earth and Space Science



## RESEARCH ARTICLE

10.1029/2021EA001884

### Key Points:

- The temperature-dependent pyrolysis kinetics of organic matter in two carbonaceous meteorites has been measured
- Meteoritic particles become slightly harder after carbon pyrolysis so only slow-moving, low density particles should fragment during entry
- Organic pyrolysis should be detectable in the head echo measured using a high performance/large aperture radar

### Supporting Information:

Supporting Information may be found in the online version of this article.

### Correspondence to:

J. M. C. Plane,  
J.M.C.Plane@leeds.ac.uk

### Citation:

Bones, D. L., Carrillo Sánchez, J. D., Connell, S. D. A., Kulak, A. N., Mann, G. W., & Plane, J. M. C. (2022). Ablation rates of organic compounds in cosmic dust and resulting changes in mechanical properties during atmospheric entry. *Earth and Space Science*, 9, e2021EA001884. <https://doi.org/10.1029/2021EA001884>

Received 10 JUN 2021  
Accepted 18 MAR 2022

### Author Contributions:

**Conceptualization:** Graham W. Mann, John M. C. Plane

**Data curation:** John M. C. Plane

**Formal analysis:** David L. Bones, Juan Diego Carrillo Sánchez, Simon D. A. Connell, Alexander N. Kulak, John M. C. Plane



**Funding acquisition:** Graham W. Mann, John M. C. Plane

**Investigation:** David L. Bones, Alexander N. Kulak, John M. C. Plane

© 2022 The Authors. Earth and Space Science published by Wiley Periodicals LLC on behalf of American Geophysical Union.

This is an open access article under the terms of the [Creative Commons Attribution License](https://creativecommons.org/licenses/by/4.0/), which permits use, distribution and reproduction in any medium, provided the original work is properly cited.

## Ablation Rates of Organic Compounds in Cosmic Dust and Resulting Changes in Mechanical Properties During Atmospheric Entry

David L. Bones<sup>1</sup>, Juan Diego Carrillo Sánchez<sup>1,2,3</sup>, Simon D. A. Connell<sup>4</sup>, Alexander N. Kulak<sup>1</sup>, Graham W. Mann<sup>5</sup> , and John M. C. Plane<sup>1</sup> 

<sup>1</sup>School of Chemistry, University of Leeds, Leeds, UK, <sup>2</sup>Now at Department of Physics, Catholic University of America, Washington DC, DC, USA, <sup>3</sup>Now at ITM Physics Laboratory, NASA/Goddard Space Flight Center, Greenbelt, MD, USA, <sup>4</sup>School of Physics and Astronomy, University of Leeds, Leeds, UK, <sup>5</sup>School of Earth and Environment, University of Leeds, Leeds, UK

**Abstract** A new experimental system is described for studying the pyrolysis of the refractory organic constituents in cosmic dust during atmospheric entry. The pyrolysis kinetics of meteoritic fragments (CM2 and CV3 carbonaceous chondrites, radius = 36–100 μm) were measured by mass spectrometric detection of CO<sub>2</sub> and SO<sub>2</sub> at temperatures between 625 and 1300 K, with most carbon being lost between 700 and 800 K. The complex time-resolved kinetic behavior is consistent with two organic components—one significantly more refractory than the other, which probably correspond to the insoluble and soluble organic fractions, respectively. The measured temperature-dependent pyrolysis rates were then incorporated into the Leeds Chemical Ablation Model, which demonstrates that organic pyrolysis should be detectable using a high performance/large aperture radar. Atomic force microscopy was used to show that although the residual meteoritic particles became more brittle after organic pyrolysis, they also became slightly harder, withstanding stresses that are at least three orders of magnitude higher than would be encountered during atmospheric entry. This suggests that most cosmic dust particles (radius <100 μm) will not fragment during entry into the atmosphere as a result of organic pyrolysis, although a subset of slow-moving, low density particles mostly from Jupiter-family comets could fragment.

**Plain Language Summary** Cosmic dust particles, particularly when they originate from comets moving into the inner solar system, are composed of silicate mineral grains bound together in a matrix of very stable organic material. During entry into a planetary atmosphere, these particles frequently heat above 800 K, at which point this organic material decomposes into mainly carbon dioxide. In this study we measured the rate of decomposition of organics in micron-sized meteoritic particles, and showed that it is fast enough that organic decomposition should be detectable by high performance radars. We also showed that the particles become slightly harder after organic decomposition, so these particles should not fragment during atmospheric entry. The exception may be slow-moving fluffy particles of the type recently observed in the ROSETTA mission to comet 67P.

## 1. Introduction

The high-speed entry of cosmic dust particles into a planetary atmosphere can have a range of impacts both in the atmosphere and at the surface. These have been reviewed both for the Earth (Plane, 2012) and other solar system bodies (Plane et al., 2017). Good progress has been made in the past decade developing chemical models of meteoric ablation, which are able to predict the ablation rates of individual elements from a cosmic dust particle of specified mass, velocity and entry angle (Vondrak et al., 2008). In the case of the Leeds Chemical Ablation Model (CABMOD), these elements include a range of metals (Fe, Mg, Si, Na, Ni etc.) (Bones et al., 2019; Carrillo-Sánchez, Gómez-Martín, et al., 2020) and P (Carrillo-Sánchez et al., 2020a). This model has been tested in the laboratory using a Meteoric Ablation Simulator (MASI-1) which enables the ablation of two elements to be observed in real time from meteoritic particles that are flash heated with a temperature profile simulating atmospheric entry (Bones et al., 2016; Gómez-Martín et al., 2017).

However, the pyrolysis of carbon and sulfur compounds in cosmic dust at temperatures below 1800 K (i.e., prior to melting), which can potentially lead to meteoric fragmentation if sufficiently rapid (Campbell-Brown, 2019),

**Methodology:** David L. Bones, Simon D. A. Connell, Alexander N. Kulak, John M. C. Plane

**Project Administration:** Graham W. Mann

**Resources:** Simon D. A. Connell, Alexander N. Kulak, John M. C. Plane

**Software:** David L. Bones, Juan Diego Carrillo Sánchez, John M. C. Plane

**Supervision:** John M. C. Plane

**Validation:** David L. Bones, Simon D. A. Connell, John M. C. Plane

**Writing – original draft:** David L. Bones, Simon D. A. Connell, John M. C. Plane

does not appear to have been considered in detail. The fragmentation of meteoroids as small as  $\sim 2$  mm in radius has been observed directly using high-speed meteor video (Campbell-Brown, 2019; Vojacek et al., 2019); observations at the Canadian Meteor Observatory (CAMO) show that a large majority ( $>90\%$ ) of the recorded meteors fragmented (Campbell-Brown, 2019). However, there are two points to keep in mind. First, in order for the fragments to be visible on video, they must be close to 1 mm in radius and not fragment further before reaching the ablation temperature above 1800 K (assuming an olivine-silicate composition (Vondrak et al., 2008)). Second, the cosmic dust particles which contribute most of the mass input to the Earth's atmosphere have radii between 10 and 200  $\mu\text{m}$  (Plane, 2012) that is, much smaller than can currently be observed optically. Note that the fragmentation of smaller particles has been inferred from oscillations in the radar head echo strength and the terminal flares of some meteors (Elford, 2004; Reddy & Premkumar, 2019; Zhu et al., 2016).

The presence of meteoric fragments may have important implications for the stratospheric ozone layer (Hoyle et al., 2013; Voigt et al., 2005) as well as aerosol layers in the stratosphere (Curtius et al., 2005; Murphy et al., 1998; Murphy et al., 2014; Schneider et al., 2021; Weigel et al., 2014). Polar stratospheric clouds are ice clouds that occur in the winter polar stratosphere and activate chlorine, leading to ozone depletion (Solomon, 1999). A long-standing problem has been to explain observations that  $\text{H}_2\text{SO}_4\text{-HNO}_3\text{-H}_2\text{O}$  droplets freeze to form solid nitric acid-containing polar stratospheric clouds (likely tri-hydrate nitric acid tri-hydrate (NAT) particles, e.g., Tolbert and Toon [2001]) at temperatures around 195 K that is,  $\sim 10$  K higher than the pure solutions (Lowe & MacKenzie, 2008). Work in our laboratory has shown that meteoritic fragments nucleate the freezing of  $\text{HNO}_3\text{-H}_2\text{O}$  droplets into NAT at these higher temperatures (James et al., 2018). Indeed, many stratospheric particles have been shown to contain refractory cores (Curtius et al., 2005; Cziczo et al., 2001; Ebert et al., 2016; Murphy et al., 1998; Voigt et al., 2005; Weigel et al., 2014), and chemical analysis (Ebert et al., 2016; Schneider et al., 2021) strongly suggests that the refractory particles are of meteoric origin.

Fragmentation may help to resolve the current problem that the flux of deposited meteoritic material in ice cores in Greenland and Antarctica appears to be more than one order of magnitude higher than can be explained from meteoric ablation rates constrained by observations of metals such as Na and Fe in the upper atmosphere (Brooke et al., 2017). This discrepancy might be explained if some of the dust particles entering the atmosphere fragmented into  $\mu\text{m}$ -sized fragments, which then sedimented rapidly into the lower atmosphere, rather than ablating. Fragmentation might also allow a greater fraction of the organic material entering an atmosphere to survive and be delivered intact to the planetary surface, which may have been important in the early evolution of planets such as Mars (Plane et al., 2017).

When a meteoroid fragments, it is reasonable to assume that some component or components of the meteoroid are responsible: either pressurized pockets of gas explosively break the particle apart, or volatile compounds evaporate or pyrolyze, thereby weakening the matrix of the meteoroid within which the primitive grains are embedded (Campbell-Brown, 2019). The tendency of fragments from large meteoroids to retain a similar trajectory to the parent body suggests the latter scenario is more typical. Indeed, interplanetary dust particles (IDPs) captured in the stratosphere include porous aggregates of silicate grains surrounded by an organic carbon mantle, termed chondritic porous IDPs (Flynn et al., 2013; Kimura et al., 2020). The types of carbon compound in these organic mantles are in general highly conjugated, aromatic groups but with significant carbonyl features and some  $\text{CH}_3$  and  $\text{CH}_2$  features (Flynn et al., 2004; Schramm et al., 1989). This has similarities with the form of carbon observed in terrestrial meteorite finds (Alexander et al., 2017; Hayatsu et al., 1977; Murae, 1997). The carbon content of IDPs is around 10 wt.% (Thomas et al., 1994). This is significantly more than the 2–5 wt.% found in primitive carbonaceous chondrites and closer to the carbon content of cometary samples (Morse & Chan, 2019). If this carbon were to pyrolyze as the particle heats on entry to the atmosphere, the aggregates could fall apart into smaller grain clusters. The parent IDP might only have to reach moderate temperatures of around 900 K to lose most of the organic carbon (Anders, 1989).

Terrestrial meteorites contain a huge variety of organic carbon, ranging from soluble, volatile hydrocarbons (termed Soluble Organic Matter, SOM) to large, refractory, insoluble macromolecular polycyclic aromatic hydrocarbon (PAH) compounds similar to the terrestrial kerogen found in oil shales (Kerridge, 1983). This latter fraction, termed Insoluble Organic Matter (IOM), accounts for about 70% of the organic carbon in a typical CM or CI meteorite (Hayes, 1967). Many compounds are highly functionalized with a number of carbonyl groups. The bulk of the compounds appear to be functionalized single cycle aromatic molecules (Cody et al., 2011). In general, the IOM in the more primitive meteorites (CM, CI, CR) is more primitive than the IOM in IDPs, and

the variety of the soluble compounds is also huge: for example, 46,000 distinct compounds were isolated from Murchison (Alexander et al., 2017; Schmitt-Kopplin et al., 2010). CM meteorites also typically contain a small fraction (around 2%) of inorganic carbonates such as calcite, aragonite and dolomite (De Leuw et al., 2010).

Very few measurements have been taken on pristine cometary dust. The Stardust mission to Wild2 returned samples that included carbon compounds with a resemblance to those found in IDPs (Rietmeijer, 2009). In general, the H/C ratio was relatively high (close to 1), indicating aliphatic compounds rather than aromatic compounds, although small amounts of the latter were also evident (Bajt et al., 2009; Clemett et al., 2010). Earlier missions to study Halley's Comet (Giotto, Vega 1 and 2) measured the dust composition by onboard mass spectrometry (Jessberger et al., 1988). H/C and O/C ratios spanned wide ranges including the low H/C and O/C regions corresponding to aromatic compounds. Measurements from the PUMA instrument on Vega 1 suggested a refractory core surrounded by organics, again similar to that observed in IDPs (Kissel & Krueger, 1987).

More recently, the Rosetta mission to comet 67P collected and analyzed particles from the coma, confirming the picture of aggregates bound together by an organic mantle (Kimura et al., 2020). The H/C ratio close to 1 suggests the organics are more saturated than those recovered from meteorites (Isnard et al., 2019). Pure aliphatic and aromatic hydrocarbons along with functionalized hydrocarbons were observed in the gas phase (Schuhmann et al., 2019). The organic and silicate phases were intimately mixed within the resolution of the instrument. The organic phase accounted for at least 45% of the total—far more than observed in IDPs or meteorites (Bardyn et al., 2017; Morse & Chan, 2019). The Rosetta particles are quite diverse (Langevin et al., 2016), but in general appear to be aggregates made of sub units about 10  $\mu\text{m}$  in radius (Hornung et al., 2016). The tensile strengths of these aggregates are estimated to be in the region of 1000s of Pa (Hornung et al., 2016).

Several previous laboratory experiments have investigated the effect on meteoritic samples of flash heating up to temperatures below their melting points. The emphasis has usually been on mineralogical changes to the particle (Greshake et al., 1998; Nozaki et al., 2006; Toppani et al., 2001), although the outgassing of volatiles ( $\text{CH}_4$ ,  $\text{CO}_2$ ,  $\text{H}_2\text{O}$  and  $\text{SO}_2$ ) has also been studied using linear temperature ramps or stepped pyrolysis studies (Court and Sephton, 2009a, 2009b, 2011; Thompson et al., 2021). A recent study by Riebe et al. (2020) flash-heated IOM extracts from the Cold Bokkeveld CM2 meteorite. At temperatures above 900 K they found significant alteration to the IOM composition, with evidence of more ordered aromatic groups and a loss of carbonyl functional groups.

In the present study we report measurements of the temperature-dependent rates of pyrolysis of organic C in meteoritic fragments. The changes in tensile strength of the particles following organic pyrolysis were also determined. We use these results to examine the likelihood that organic pyrolysis leads to fragmentation during atmospheric entry, and to predict whether organic pyrolysis could be observed using a High Performance Large Aperture (HPLA) radar.

## 2. Experimental

### 2.1. Pyrolysis Kinetics

The new Meteoric Ablation Simulator-2 (MASI-2) developed for this study, which consists of a vacuum chamber coupled to a mass spectrometer, is illustrated in Figure 1. Inside the chamber is a heated plate (red block in Figure 1). The aim of the study was to flash heat the particles to mimic the heating of micrometeoroids on atmospheric entry. Previously we used a tungsten filament to heat particles up to 2800 K, in order to study the ablation of refractory metals (Bones et al., 2016). In the present study, to reproduce the lower temperatures relevant to pyrolysis of organic compounds, we decided that dropping the particles onto a hot plate would reproduce the temperature profile more closely. Samples are held in a hopper above the platform until it reaches the required temperature, at which point the sample is released and funneled onto the hot plate. The plate surface consists of Omega bond cement, with a coiled NiChrome wire (length = 1 m, diameter 0.25 mm, resistance  $\sim 35 \Omega$ ) embedded in it. The surface can be resistively heated to around 1350 K, above the upper limit of 1300 K required for these experiments. Typically 5–10 mg of particles were dropped onto the hot plate, so that the grains were spread in a single layer over it. The plate consists of a flat region surrounded by a lip to contain the particles once they have been dispensed. Note that if any powder missed the hot plate during the drop, then it would not have contributed to the change of  $\text{CO}_2$  in the chamber.

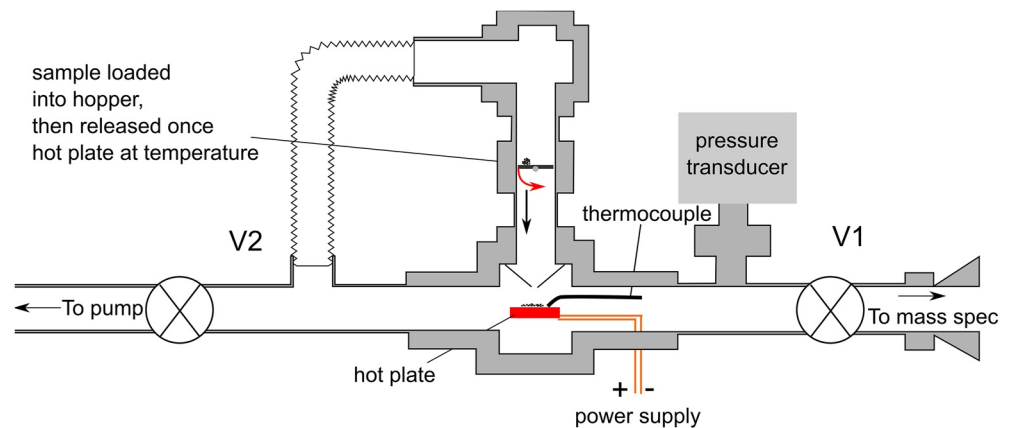


**Figure 1.** Schematic diagram of the ablation chamber in the MASI-2 instrument.

The chamber can be pumped down to below 1 mTorr (0.13 Pa), as measured using an MKS Baratron. Ablation is observed to start in the atmosphere around a pressure of  $1 \times 10^{-6}$  bar (Plane et al., 2015), so the chamber was at a pressure consistent with what a meteoroid would experience on entering the atmosphere.  $O_2$  could also be added to the chamber to test the effect on pyrolysis rates. A Hiden HPR60 quadrupole mass spectrometer was used to analyze the gases emitted from the heated samples. A single mass could be monitored at a rate of 6 Hz; alternatively, scanning from  $m/z = 10$ –120 amu could be carried out at 0.07 Hz. Note that we are assuming the ions produced in the mass spectrometer are singly charged. Gases produced in the MASI-2 chamber were pumped past the orifice of the mass spectrometer using a roots blower (Edwards EH500 A) backed by a large displacement rotary pump (Edwards E2M80). This ensured that any gas produced was sampled with negligible delay using the mass spectrometer.

The temperature of the hot plate surface is measured using a K-type bare wire thermocouple (AWG8, from Omega). The tip of the thermocouple rests on the heated surface near the point where the particles are deposited. The temperature measured using the thermocouple was significantly lower than the actual surface temperature experienced by the particles, and so the thermocouple was calibrated with several substances of known melting point (two types of solder and antimony with melting points between 470 and 1300 K), and a pyrometer (System 4 Ratio Thermometer and Land Instruments) for temperatures above 1300 K. The error in the linear fits for the thermocouple calibration equates to around  $\pm 25$  K on average for the hot plate temperatures.

## 2.2. Cosmic Dust Proxies

In the MASI-2 experiments, two IDP analogs were used: samples of the Jbilet Winselwan (JW) and Allende meteorites. JW is a carbonaceous chondrite of CM2 classification notable among CM2 meteorites for its lack of carbonates, which in turn suggests little hydrous alteration (Grady et al., 2014). Otherwise, in terms of elemental composition, general mineral compositions and oxygen isotope ratios it is typical of the CM2 category (Ruzicka et al., 2015), a characterization confirmed by the detailed analysis conducted by Friend et al. (2018). JW is therefore a relatively primitive, carbon-rich meteorite that was the closest available match to cometary dust. Cometary dust accounts for up to 90% of the cosmic dust particles entering the Earth's atmosphere (Carrillo-Sánchez et al., 2016) and is expected to have a composition similar to primitive chondrites, albeit less dense and with a much higher carbon content. JW is 2% organic carbon (King et al., 2019), which is far less than has been measured in cometary dust samples: Rosetta particles, for example, are  $\sim 45\%$  C (Bardyn et al., 2017; Morse & Chan, 2019). However, we think it likely that the carbon-containing compounds present in JW are representative of those found in cometary dust, due to the relatively pristine nature of JW, as evidenced by its CM classification. While there is some evidence of thermal alteration of JW, King et al. (2019) consider JW to have been heated to no higher than 770 K, which is below the temperature at which we expect most of the C containing compounds to pyrolyze (Section 3).

To conserve the limited supply of JW, a piece of oil shale was obtained from the British Geological Survey (sample: Metherhills 1 SSK104938, Core 265200). The organic carbon in oil shale is largely in the form of

kerogen (Kerridge, 1983), as in meteorites. The pyrolysis of carbon from oil shale has also been extensively studied, providing a useful benchmark for our experimental results. Therefore, we used the oil shale sample as a meteorite proxy for these experiments.

The second meteorite sample was the CV3 carbonaceous chondrite Allende. This has a C content of 0.29 wt% (bulk) (Jarosewich, 1990), which is significantly lower than the 1.99 wt% C content of JW (King et al., 2019). The oil shale and the meteorite samples were ground to a coarse powder in an agate mortar and pestle, then size selected using an Endecott test sieve. This resulted in bins of particles with average radii of 36, 64 and 100  $\mu\text{m}$  ( $\pm 50\%$ ). A total of 34 samples from the two meteorites and the oil shale sample were analyzed. See Table S2 in Supporting Information S1 for details.

### 2.3. Experimental Protocol

Samples were first loaded into the upper chamber of the MASI-2 (Figure 1), which was then sealed and pumped down to a pressure  $< 1$  mTorr. At this point, the gate valve to the mass spectrometer was opened, and the hot plate temperature ramped up to 1150 K over 25 min, whilst the  $\text{CO}_2$  concentration was monitored using the mass spectrometer at  $m/z = 44$  amu. This allowed any remaining residue to be baked off the heater. The hot plate temperature was then lowered to a selected temperature between 600 and 1100 K (for experiments involving meteoroid proxies). Once the temperature had been stable for 30 s and the  $\text{CO}_2$  background was stable, the sample was released onto the hot plate. This resulted in an immediate rise in the  $\text{CO}_2$  signal as the carbon in the sample began to pyrolyze. After 60 s, the hot plate temperature was raised rapidly to 1150 K. After allowing a further 1,140 s for any remaining carbon to pyrolyze, the experiment was terminated. Increasing the bakeout temperature of the hot plate did not produce an appreciable rise in the  $m/z = 44$  signal. Examples of the  $m/z = 44$  signal are included in the Supporting Information (Figure S3 in Supporting Information S1), and show a drop to a stable background level after 300–500 s.

The  $\text{CO}_2$  time-profiles were background corrected using the  $\text{CO}_2$  signal during the 30s before sample release. The cumulative signal was then normalized to the total  $\text{CO}_2$  emitted from the particles. In this manner, the cumulative signal is equivalent to the fraction of carbon-containing compounds lost. JW is known to have only very small amounts of inorganic carbon (Grady et al., 2014), so in this case the signal is equivalent to the organic mass lost.

Experiments were also conducted where the samples were placed on the hot plate at room temperature, and then a slow linear heating ramp of  $\sim 16$   $\text{K min}^{-1}$  from 293 to 1300 K was applied, with the mass spectrometer continuously scanning from  $m/z = 10$ –127 amu, with the pressure in the chamber being maintained at 0.1 Torr. Each ramp heating experiment was preceded by a blank experiment to measure the ablation of residual chemical species. Although flash heating is more representative of meteoroid entry than ramp heating, it is only practical for one compound (i.e., one  $m/z$  value) at a time to achieve good time resolution; whereas ramp heating provides a general, qualitative picture of the ablating compounds and the temperatures at which they ablate. Lastly, a thermogravimetric analysis (TGA) (Ozawa, 1965; Kar & Hascakir, 2017; Vyazovkin, 1996) was performed on the oil shale and JW meteorite particles (see the Supporting Information for further details).

### 2.4. AFM Yield Stress Tests

Atomic Force Microscopy (AFM) was performed using a Nanoscope 8 Multimode (Bruker) on samples of oil shale and JW meteorite, both before and after heat treatment at 925 K. For the AFM analysis, the particles were firmly mounted in a thin layer of 2-part epoxy resin on metal stubs. Yield stress tests were conducted on a minimum of 4 regions of 6–10 particles per sample. Each area was only probed once, as only 5 repeated measurements in the same location results in a compacted hole in the surface with no measurable indentation and high adhesion. The AFM is equipped with a top down camera for location of the probe. FESPA AFM probes (Bruker Probes, nominal spring constant of  $2.8$   $\text{N m}^{-1}$ ) were used in the contact mode, under air.

The spring constant of the cantilever was measured using the thermal noise method (where the power of the thermally driven deflection fluctuations are proportional to the spring constant and temperature), and the Sader method (which uses knowledge of the probe geometry and materials together with its resonant frequency and Quality factor). The spring constants were in the range  $1.2$ – $2.6$   $\text{N m}^{-1}$ , and the values obtained by the two methods were typically within 5% of one another.

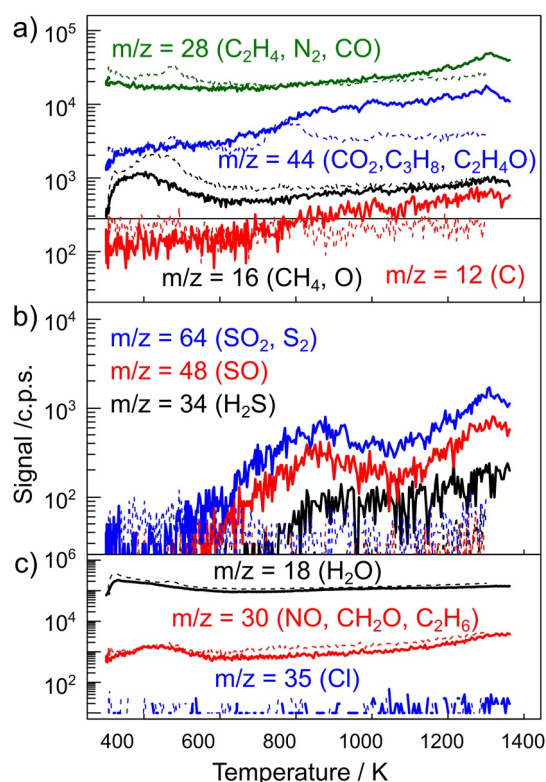


**Figure 2.** Signal profiles of gases emitted during a linear heating ramp ( $16 \text{ K min}^{-1}$ ) of  $100 \mu\text{m}$  Jbilet Winselwan meteorite particles. Dotted lines: blank profiles (i.e., with no sample loaded). (a) Profiles attributed to C-containing compounds. (b) Profiles attributed to S-containing compounds. (c) Other profiles.

with the meteorite samples. Figure 2a shows the detection of four different carbon species from the JW meteorite. The production rates of molecules with masses corresponding to  $m/z = 12$  and  $44$  amu clearly increase above the blank at temperatures  $>800 \text{ K}$ , possibly reaching a maximum before the linear ramp is terminated at  $1350 \text{ K}$ . Mass 12 is unambiguously C and the correspondence of its profile with mass 44 lends confidence to the assignment of  $\text{CO}_2$  to mass 44, although it is possible that there are contributions from other carbon-containing species ( $\text{C}_3\text{H}_8$  and  $\text{C}_2\text{H}_4\text{O}$ ). Mass 28 is likely to be from background  $\text{N}_2$ , although contributions from  $\text{CO}$  and  $\text{C}_2\text{H}_4$  cannot be ruled out.  $\text{CO}_2$  fragments into C and CO during electron impact ionization at  $70 \text{ eV}$ , with both fragments around 10% abundance of the parent peak (NIST Mass Spectrometry Data Center, 2020). The temperature profiles of the carbon-containing compounds are in satisfactory agreement with those observed recently by Thompson et al. (2021) during their linear temperature ramps on meteorites including JW.

The mass profiles of three likely sulfur compounds (masses 34, 48 and 64) are depicted in Figure 2b. Mass 64 could be either  $\text{S}_2$  or  $\text{SO}_2$  although the latter is much more likely as an oxidation product of released sulfur or sulfides. This is confirmed by the mass 64 profile tracking that of mass 48 that is,  $\text{SO}_2$  fragmenting to form SO, consistent with the mass spectral database (NIST Mass Spectrometry Data Center, 2020).  $\text{SO}_2$  should also fragment to S, with mass 32 amu, but at around 12% of the  $\text{SO}_2$  parent peak, this fragment is likely lost in the noise from background  $\text{O}_2$ . Mass 34 exhibits a slightly different profile. It is probably  $\text{H}_2\text{S}$  evaporating directly from the meteorite particles. All of these sulfur profiles show a double peak, initially around  $900 \text{ K}$  (slightly later for  $\text{H}_2\text{S}$ ) followed by a rise to a maximum at  $1300 \text{ K}$ , before the linear ramp was halted at  $1350 \text{ K}$ .

Sulfur is present in carbonaceous chondrites at around 2–3 wt.% (Court & Sephton, 2011). The total sulfur released in the linear ramp depicted in Figure 2, was approximately seven times lower than the total carbon (once the relative ionization cross sections of  $\text{CO}_2$ ,  $\text{SO}_2$  and  $\text{H}_2\text{S}$  had been corrected for). This calculation relies on

The surface stress generated by the tip depends on the normal force and the tip radius, and this value can change with wear. The tip radii of a range of previously used probes were estimated by running the AFM in the Peak Force–Quantitative Nanomechanical Mapping (PF-QNM) mode on a low density polyurethane standard sample of known modulus. With all other parameters calibrated, the tip radius is the only free adjustable parameter to achieve the correct elastic modulus. A total of seven probes that all had a tip radius in the range of  $30 \pm 5 \text{ nm}$  were selected for the indentation measurements. Force indentation curves were controlled using a relative trigger set to  $100 \text{ nN}$ , but if this force was not sufficient to cause the surface to indent or yield it was increased in further  $100 \text{ nN}$  increments (starting with a trigger set too high leads to continuous penetration into the particle). The samples were studied over a period of 2 months, and multiple probes were used for the same samples, introducing the maximum amount of repeatability the seven different probes used. On average, each sample was measured using three probes. Data was analyzed using Nanoscope Analysis v9.1 software (Bruker).

### 3. Experimental Results and Discussion

#### 3.1. Organic Pyrolysis

##### 3.1.1. Mass-Resolved Gas Analysis From Linear Temperature Ramps

When samples of the two meteorites were subjected to linear temperature ramps ( $293\text{--}1300 \text{ K}$ ), unambiguous releases of carbon- and sulfur-containing compounds were observed. Other species, possibly including nitrogen- and chlorine-containing compounds, were also emitted but cannot be identified unambiguously. The detection of species from the linear temperature ramp experiments was less certain than experiments where the sample was dropped onto the hot plate already set to an elevated temperature. This is due to the signal being lower and more variable over the hour-long duration of the heating ramp as well as the presence of residual contamination on the heater surface. Blank experiments were therefore also run to compare

many assumptions, the main ones being that masses 28 and 44 are entirely due to carbon compounds (i.e., CO and CO<sub>2</sub>). However, it is clear that much more carbon than sulfur is detected at temperatures lower than 1300 K. The presence of H<sub>2</sub>S suggests that there may be insufficient oxygen present to oxidize all the sulfur compounds produced. Note that sulfates present in the meteorite samples (mostly CaSO<sub>4</sub> and MgSO<sub>4</sub>) would not decompose at temperatures below 1300 K (see Table 2 of Court and Sephton [2014]).

Water ( $m/z = 18$ ) is present as a contaminant in the chamber. It is clear that essentially all of the H<sub>2</sub>O is desorbing from surfaces in the chamber, as the blank run in Figure 2c (dashed black line) closely matches the sample run (solid black line). All the TGA analyses show an initial step, which can be attributed to H<sub>2</sub>O loss from the actual sample (the thermal analyzer has a blank cuvette analyzed in parallel with the sample cuvette). This H<sub>2</sub>O is likely to be both from H<sub>2</sub>O adsorbed during sample preparation and H<sub>2</sub>O locked in the silicates of the meteorite (e.g., from the decomposition of serpentine (Court & Sephton, 2014)).

Figure 2c also shows the temperature profiles of masses 30 and 35. Mass 35 is not an isotopologue of H<sub>2</sub>S because its abundance would be less than 1% of the H<sub>2</sub>S signal and hence not detectable. The most likely candidate is Cl. Mass 30 is ambiguous. The peak at low temperatures is likely to be contamination (from an experiment involving ammonium nitrate). The signal from  $m/z = 16$  is likely from background O<sub>2</sub>, since it closely matches the  $m/z = 28$  signal (attributed to N<sub>2</sub>) at low temperatures.

The masses displayed in Figure 2 are chosen because they are either species of interest or their mass profiles show unambiguous peaks or rises at high temperatures. The linear ramp analyses suffer from the disadvantage of noisy backgrounds and a lack of reproducibility. One experiment avoided these issues by dropping a sample of oil shale onto the hot plate at 1000 K, and monitoring the change in signal for masses between 27 and 127 amu. Many masses showed a clear increase when the sample was dropped, indicating emission from the sample. However, mass 40, which corresponds to <sup>40</sup>Ar, did not change when the sample was dropped onto the hot plate, indicating that Ar came entirely from leaks into the chamber. A few masses showed sharp, short-lived peaks. These were masses 35, 48 and 64, suggesting that volatile chlorine and sulfur ablated rapidly.

### 3.1.2. Pyrolysis Rates From Flash Heating Experiments

The MASI-2 chamber allows the rates of carbon pyrolysis from meteoroid proxies to be measured from the time-resolved production of  $m/z = 44$ , corresponding to CO<sub>2</sub> (Section 2.3). The majority of carbon produced by pyrolysis combusts to CO<sub>2</sub>. The maximum rate of CO<sub>2</sub> production, normalized to the total CO<sub>2</sub> ablated, was extracted from each experiment. Plots of the raw  $m/z = 44$  signal are included in the SI (Figure S2 in Supporting Information S1). Figure 3a compares Arrhenius plots of the pyrolysis rates for the two carbonaceous chondrites (average particle radius = 100 μm). The Arrhenius parameters for JW and Allende are the same, within their 1σ errors. Given that CO<sub>2</sub> is the major carbon-containing pyrolysis product, the fugacity of O<sub>2</sub> in the chamber could be a rate-limiting factor. To test this, the JW measurements were repeated with added O<sub>2</sub> at a pressure of 2.7 Pa (i.e., at least 100 times the background O<sub>2</sub> in the chamber). Figure 3b shows that the production rates of CO<sub>2</sub> in the presence and absence of O<sub>2</sub> are the same within error. Since the small amount of O<sub>2</sub> present is insufficient to combust most of the carbon compounds formed by pyrolysis (Court & Tan, 2016), secondary reactions must be taking place within the particle, for example, oxidation of C via reduction of FeO or Fe<sub>2</sub>O<sub>3</sub> (Genge & Grady, 1998; Cordier et al., 2011). Note that an O<sub>2</sub> pressure of 2.7 Pa corresponds to an altitude of around 62 km in the Earth's atmosphere, which is well below the height at which ablation occurs (Carrillo-Sánchez, Gómez-Martín, et al., 2020). This implies that O<sub>2</sub> atmospheric fugacity should not play a role in the kinetics of organic pyrolysis in cosmic dust during atmospheric entry.

There is also no clear trend in the CO<sub>2</sub> production rate from pyrolysis with particle size, as shown in Figure 3c, which compares the Arrhenius plots for JW samples of 36, 64 and 100 μm radius. This indicates that diffusion of CO<sub>2</sub> out of the particles is not rate-limiting. Previous experiments on the ablation of metals such as Ni and Na show that the ablation rates are also largely independent of particle size (Bones et al., 2019).

The rates of ablation of the JW chondrite particles can also be compared with those of the oil shale sample (Figure 3d). While the carbonaceous chondrites show little difference in their Arrhenius plots, the oil shale sample exhibits a significantly steeper temperature dependence, which is consistent with the faster, earlier release of carbon observed from the TGA profiles of the JW particles (see Figure S1 in Supporting Information S1).

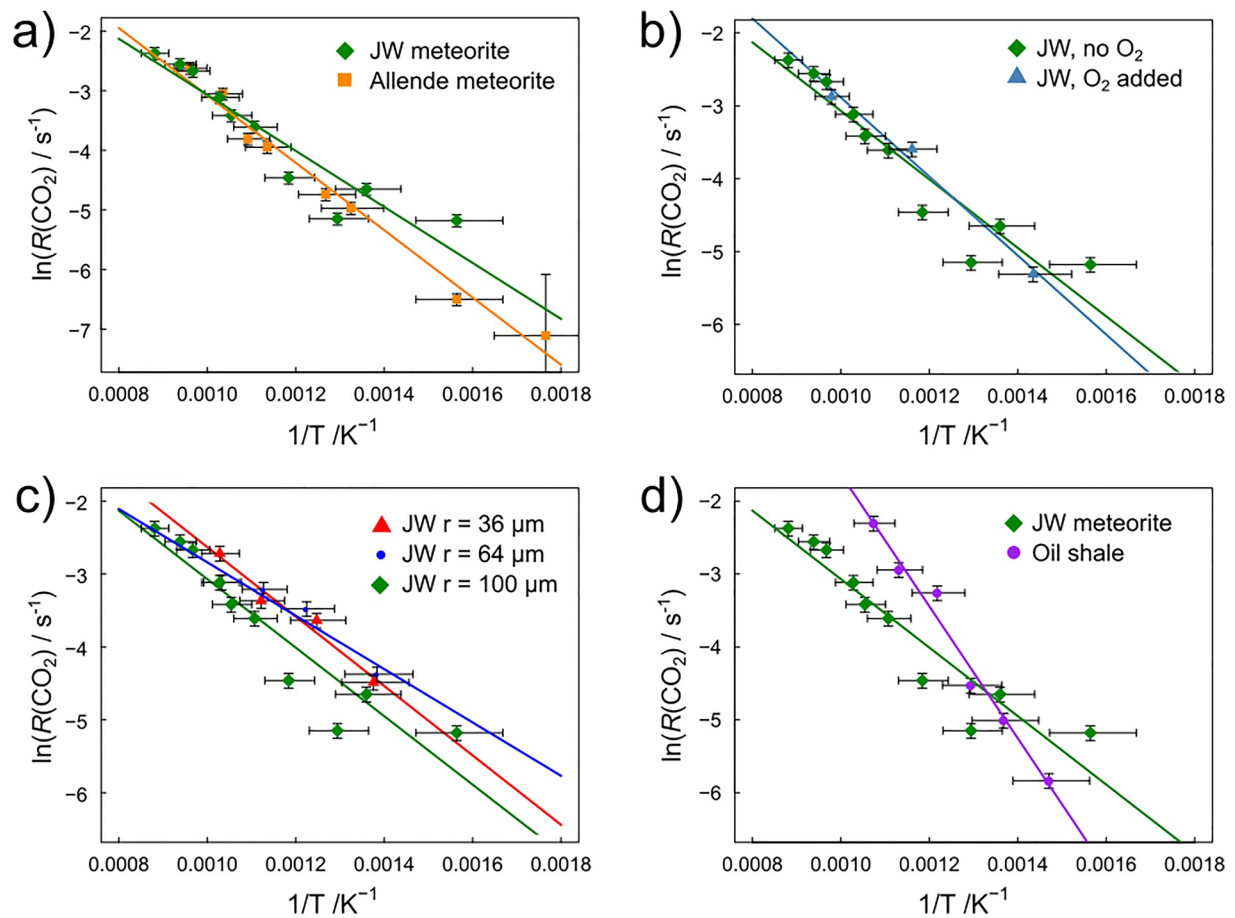


**Figure 3.** Arrhenius plots of the normalized maximum  $\text{CO}_2$  production rate versus  $1/T$  (the solid lines are fitted linear regressions through the data points): (a) Comparison of flash-heated Jbilet Winselwan (JW) (CM2, green diamonds) and Allende (CV3, orange squares) particles of 100  $\mu\text{m}$  radius, which agree within error for these carbonaceous chondrites; (b) Comparison for flash-heated 100  $\mu\text{m}$  JW particles  $[\text{O}_2] = 2.7 \text{ Pa}$  (blue triangles) or  $[\text{O}_2] < 0.026 \text{ Pa}$  (green diamonds); (c) Comparison of flash-heated JW particles of average radius 36  $\mu\text{m}$  (red triangles), 64  $\mu\text{m}$  (blue circles) and 100  $\mu\text{m}$  (green diamonds); (d) Comparison of flash-heated JW (green diamonds) and terrestrial oil shale (purple circles) 100  $\mu\text{m}$  particles.

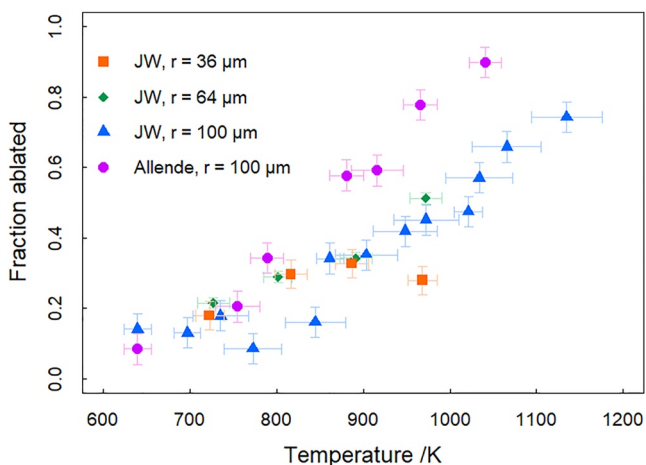


**Figure 4.** Fraction of organic carbon ablated during flash heating experiments as a function of temperature for four meteorite samples (see legend).

The fraction of pyrolyzed organic carbon from JW and Allende particles is shown as a function of temperature in Figure 4. In each case, the samples were dropped onto the preheated hot plate for 60 s. This period of time was generally sufficient to pyrolyze all of the organic carbon that would decompose at the target temperature, as evidenced by the  $\text{CO}_2$  signal dropping to the background level. In the few cases where the signal did not decay to the background, the pyrolysis fraction was estimated by modeling an exponential decay to the mass 44 signal, and extrapolating until the  $\text{CO}_2$  signal was within 1% the background level. This procedure takes into account all the  $\text{CO}_2$  that would have been produced at the test temperature, and typically accounted for an additional 5%–10% of  $\text{CO}_2$ . Both meteorites show a roughly linear trend of pyrolysis fraction versus temperature. The JW data with three particle sizes also show that there is essentially no size dependence on the fraction that pyrolyzes at each temperature.

### 3.2. Yield Stress Measurements

Figure 5 is an overlay of two representative approach indent curves (all the retract curves are removed for clarity) for each of the samples. The oil



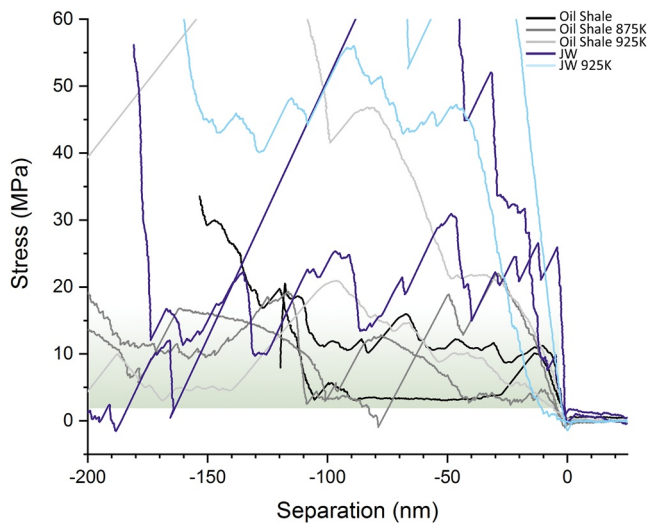


**Figure 5.** AFM yield stress measurements, showing representative approach indent curves for each of the samples referred to in the legend (all the retract curves are removed). The zone where the low yield stress fractures occur is shaded in green.

shale samples are colored from black to gray (going from unheated to heat-treated particles at 875 and 925 K), and the JW samples in blue to light blue (unheated to heat-treated at 925 K). More examples are given in Figure S4 in Supporting Information S1 with several approach and retract curves shown for each sample (Figure 5 is included as the bottom right panel in Figure S4 in Supporting Information S1 but scaled to show the full extent of the data).

The probe is moving to the left on the separation axis, with zero separation representing contact, and negative separation is the probe nanoindentation. After contact the force rises rapidly, the gradient of this line is a measure of elastic modulus, with the probe indenting up to 10 nm before yielding. At the yield stress the force curve exhibits a sudden load drop, characteristic of the sudden failure or fracture of a brittle or friable material. Small scale load drops during AFM-based nanoindentation have been observed on metals and attributed to atomic dislocations (Bufford et al., 2014), which have recently been modeled in detail (Ananthakrishna & Krishnamoorthy, 2018). Micro and nanoindenters with probes larger than an AFM tip have measured force curve excursions on oil shale (Han et al., 2018; Su et al., 2019), that are termed ‘pop-ins’, which are essentially the same signal of a sudden failure but measured over a broader area, which prevents the probe falling into the new fissure.

The zone where the general low yield stress fractures occur is shaded in green in Figure 5. This zone is in the 3–10 MPa range for the oil shale, and a bit higher for the JW particles. All the samples are highly heterogeneous, and the probe regularly hit hard regions at random points, but again these fracture at higher stress on JW than on oil shale. Occasionally a region is encountered in all samples that cannot be fractured with the probes used; these are most likely small hard inclusions or grains. On the first contact, the JW (blue curves) rises more steeply than the oil shale, which indicates that the surface is stiffer before fracture. Qualitatively, JW has a higher modulus and yields at higher stress, typically in the range 40–80 MPa with more severe and deeper fracture, although it is still in the same vicinity as the oil shale. This implies that the JW is harder and more brittle than the oil shale; the latter typically yields almost as a soft continuous matrix in the range 3–20 MPa with the odd hard inclusion.

After heating, the fracture forces appear to increase for both samples on average (there is still a wide spread of values that overlap). However, the initial slope is less vertical, indicating that the surface modulus decreases. There are a few points when the traces fall down to zero and have a few very low yield stress fractures immediately afterward. These are huge load drop events where the material fractures, and the probe falls 100 nm or so, with the load going to zero, but the probe will then strike the new surface with a high velocity and impact. When this happens (the long diagonal straight lines moving top right to bottom left), each time there are a few small events that follow as the force rises again up to the baseline level. These are likely caused by fragments from the damaged surface, and since this behavior is repeated each time a big fracture occurs, they should be discarded when establishing the lowest stress level. These very large load drops indicate that the particles have become more brittle after heating, with much larger and deeper failures once the yield stress has been exceeded. Finally, the depth of penetration in the heated JW particle is limited to around 100 nm before forces rise beyond the maximum force applied, again indicating that overall the material is tougher after heating (Figure S4d in Supporting Information S1).

Although the JW is stiffer and exhibits a higher yield stress overall than the oil shale, and the yield stress of both increase significantly after experiencing high temperature, it is likely that the fragmentation properties of the overall particle are more influenced by the lower end of the yield stress distribution. In other words, what is the weakest pressure measured that causes a load-drop fracture event? The lowest initial yield points, taken from the distribution of all particles examined, were 3.0 and 3.1 MPa for the oil shale unheated and heated to 925 K, respectively. In the case of JW particles, these yield points were somewhat lower, 1.2 and 1.9 MPa for unheated and 925 K, respectively. That is, the yield stress of the particles did not change significantly after organic pyrolysis. Note that these stresses are much larger than the maximum pressure of 500 Pa encountered by cosmic dust particles ( $r < 200 \mu\text{m}$ ) during atmospheric entry (Brooke et al., 2017).

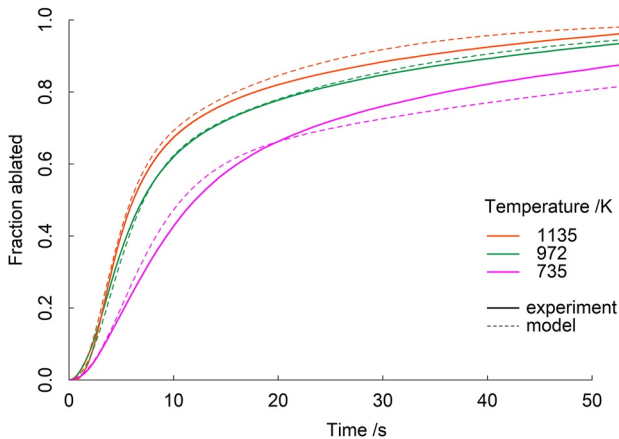


**Figure 6.** Examples of the time-resolved ablation of CO<sub>2</sub> at three different temperatures for JW meteorite particles ( $r = 100 \mu\text{m}$ ). The ordinate axis is the fraction of carbon (SOM and IOM) ablated at the specified temperature of the hot plate. The experimental profiles are the solid lines at three representative temperatures (735, 972 and 1135 K), and the model fits are shown with dashed lines corresponding to the same three temperatures.

## 4. Discussion

### 4.1. Organic Pyrolysis Kinetics

The pyrolysis of CO<sub>2</sub> from the meteorite particles was modeled by developing the evaporation model of Saleh et al. (2017). This model essentially assumes that the change in temperature of a particle is due to both the heat transferred to the particle from the hot surface and the change in latent heat due to mass evaporation. However, in the case of meteorites with at most 2 wt.% carbon, cooling due to the emission of CO<sub>2</sub> produced by pyrolysis will be negligible and so the cooling effect of latent heat of evaporation was not included. The effective conductivity of the particles constrains the rate of heat transfer from the hot plate surface to the particle and this accounts for the initial lag in the CO<sub>2</sub> production seen in the experimental MASI-2 profiles (Figure 6).

It is evident from the time-resolved CO<sub>2</sub> emission profiles, which do not exhibit single exponential growth, that at least two carbonaceous components are involved, one relatively volatile and the other relatively refractory. These probably correspond to the SOM and IOM components in IDPs and meteorites (see Section 1). We therefore fed the particle temperature from the evaporation model into the following kinetic expression, which included two terms to account for the fraction of organic carbon ablated:

$$\text{Fraction ablated} = f_{\text{SOM}} [1 - e^{-k_{\text{SOM}}t}] + f_{\text{IOM}} [1 - e^{-k_{\text{IOM}}t}]$$

where  $f_{\text{SOM}}$  and  $f_{\text{IOM}}$  are the fraction of soluble and insoluble organic material in the particles, and  $k_{\text{SOM}}$  and  $k_{\text{IOM}}$  are the first-order rate constants for organic pyrolysis, respectively. The model parameters were manually adjusted to get the best match between the modeled and experimental profiles, of which a subset are illustrated in Figure 6. This yields

$$f_{\text{SOM}} = 0.59; k_{\text{SOM}}(T \geq 625 \text{ K}) = 2.5 e^{-(2100/T)} \text{ s}^{-1}$$

$$f_{\text{IOM}} = 0.41; k_{\text{IOM}}(T \geq 625 \text{ K}) = 2.9 e^{-(3700/T)} \text{ s}^{-1}$$

Note that these pyrolysis rates determined from the model are somewhat higher than the maximum measured rates plotted in Figure 3. This is because the lag caused by heat transfer from the hot plate surface to the particles means that the maximum CO<sub>2</sub> production rate is delayed (Figure 6) and is therefore lower than if the particle had instantaneously reached the plate temperature. The SOM and IOM fractions are in reasonable accord with measurements in primitive meteorites of 70% and 30%, respectively (Hayes, 1967). Further details of the model and a list of the optimized model parameters are provided in the Supporting Information.

### 4.2. Ablation During Atmospheric Entry and Resulting Radar Cross Sections

The organic pyrolysis rate coefficients (Section 4.1) can now be used in the CABMOD model (Carrillo-Sánchez, Gómez-Martín, et al., 2020) to predict the atmospheric ablation profile of organic carbon. First, we need to make assumptions about the pyrolysis rates in the temperature ranges outside the measured range. Below 625 K, where pyrolysis was too slow to observe in the MASI-2 instrument, we arbitrarily increased the activation energy to  $E_{\text{act}}/R = 7400 \text{ K}$ , and set the pre-exponential factor so that the rates at 625 K are equal to the rates obtained from the kinetic model fit to the experimental data in Section 4.1. The resulting  $T$ -dependent rate coefficients at low temperatures are then

$$k_{\text{SOM}}(T < 625 \text{ K}) = 1.2 \times 10^4 \exp(-7400/T) \text{ s}^{-1}$$

$$k_{\text{IOM}}(T < 625 \text{ K}) = 1.1 \times 10^3 \exp(-7400/T) \text{ s}^{-1}$$

These expressions give e-folding lifetimes for SOM and IOM of  $7.0 \times 10^9$  and  $7.8 \times 10^{10}$  yrs at 150 K that is, slightly longer than the age of the solar system (which is required for the organic matrix to survive). Such

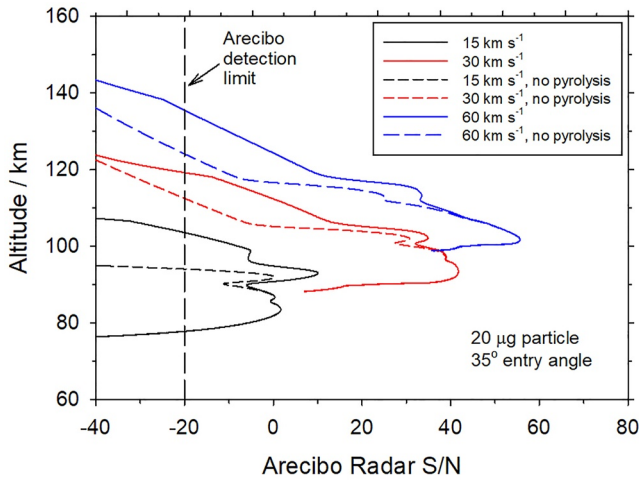


**Figure 7.** The radar S/N predicted as a function of height for the Arecibo HPLA radar observing a 20  $\mu\text{g}$  cosmic dust particle entering the atmosphere at 35° to zenith and three different velocities (see legend). The solid lines include organic pyrolysis as well as the ablation of metals, whereas the dashed lines show the case where no organic pyrolysis occurs.

an increase in activation energy is not surprising since carbon (and sulfur) pyrolysis involves a complex set of chemical reactions and physical transport through the particle.

We assume that once the temperature of a particle reaches 1800 K and the silicate grains start to melt, the pyrolysis rate of any remaining organics will increase significantly. The pyrolysis rates for SOM and IOM were therefore increased arbitrarily by a factor of 20. This ensures that the remaining carbon evaporates along with the metals and silicon. The same sigmoid function that we have derived previously from laboratory studies of the melting of carbonaceous chondritic fragments (Bones et al., 2019), centered at 1800 K with a width of 51 K, was applied to smoothly ramp up the increase in the pyrolysis rate.

We now consider whether the release of  $\text{CO}_2$  and  $\text{SO}_2$  from a cosmic dust particle entering the atmosphere would be detectable by a HPLA radar, such as the Arecibo 430 MHz radar (Janches et al., 2014). As an example, consider a 20  $\mu\text{g}$  particle with a carbon content of 10 wt.%, and an SOM/IOM ratio = 0.59/0.41 (Section 4.1). This mass is close to the maxima in the mass distributions of particles from Jupiter-family and Long-period comets as well as the asteroid belt (Carrillo-Sánchez, Gómez-Martín, et al., 2020). The particle enters the atmosphere at 35° to zenith, at speeds of 15, 30 and 60  $\text{km s}^{-1}$ .

The ionization probability of the  $\text{CO}_2$  that ablates can be calculated using the formalism developed by Janches et al. (2017). The ionization efficiency  $\beta_0$  is expressed as a function of impact velocity  $V$  by

$$\beta_0(V) = \frac{c(V - V_0)^2 V^{0.8}}{1 + c(V - V_0)^2 V^{0.8}}$$

where  $V_0$  is the threshold velocity, given by

$$V_0 = \sqrt{\frac{2(M_X + M_a) \cdot e \cdot \psi(X)}{M_X M_a}}$$

$M_X$  and  $\psi(X)$  are the mass and ionization potential of the species of interest ( $X = \text{CO}_2$  or  $\text{SO}_2$ ), respectively,  $e$  is the electronic charge, and  $M_a$  is the molecular mass of  $\text{O}_2$  or  $\text{N}_2$ .  $C$  is a fitted parameter, which is estimated relative to that for the collisional ionization of Fe:

$$c(X) = c(\text{Fe}) \times \left[ \frac{\psi(\text{Fe})}{\psi(X)} \right]^2$$

where  $c(\text{Fe}) = 1.97 \times 10^{-15} (\text{km s}^{-1})^{-2.8}$  is obtained from fitting to recent experimental data ( $\psi(\text{Fe}) = 7.90 \text{ eV}$ ) (Thomas et al., 2016). For  $\text{CO}_2$ ,  $\psi(\text{CO}_2) = 13.78 \text{ eV}$ ,  $V_0 = 12.36 \text{ km s}^{-1}$  and  $c(\text{CO}_2) = 6.47 \times 10^{-16} (\text{km s}^{-1})^{-2.8}$ ; and for  $\text{SO}_2$ ,  $\psi(\text{SO}_2) = 12.35 \text{ eV}$ ,  $V_0 = 10.95 \text{ km s}^{-1}$  and  $c(\text{SO}_2) = 8.06 \times 10^{-16} (\text{km s}^{-1})^{-2.8}$ .

For a molecule (or atom) that ablates from a sufficiently high velocity particle, successive collisions as it loses momentum may lead to ionization. The overall ionization efficiency is then given by Jones (1997):

$$\beta_{ip}(V) = \beta_0(V) + 2 \int_{V_0}^V \frac{\beta_0(V')}{V'} dV'$$

The resulting radar S/N for Arecibo can then be estimated using the method described by Janches et al. (2014). For this calculation we include an  $\text{SO}_2$  pyrolysis rate which is set to 11% of the  $\text{CO}_2$  rate (assuming the particle has a 3 wt.% S content (Court & Sephton, 2011)).

Figure 7 shows the predicted S/N as a function of altitude for three different entry velocities, and with organic pyrolysis either included, or turned off. This demonstrates that the ablation of  $\text{CO}_2$  should make a significant

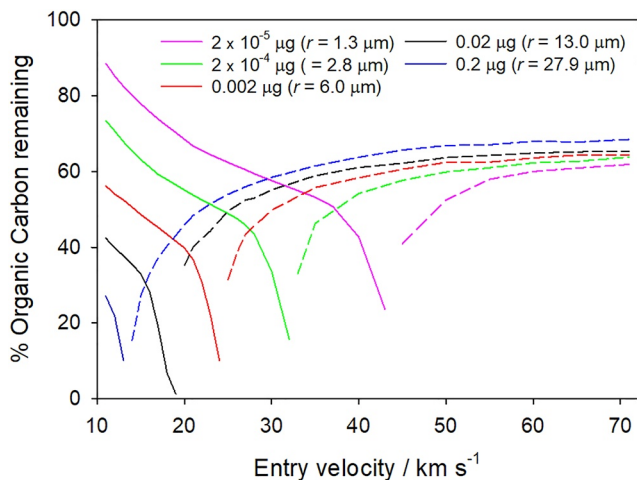


**Figure 8.** Percentage of organic carbon remaining in a dust particle as a function of entry velocity (zenith entry angle = 35°). The results are shown for 5 masses ranging from  $2 \times 10^{-5}$  to  $0.2 \mu\text{g}$ . For each mass, the solid line shows the organic fraction remaining if the particle does not reach the melting point (1800 K) during entry. The dashed line in the same color shows the organic fraction present at the point of melting if the particle heats to above 1800 K.

difference to the topside of the radar profile, above the narrow peak in the profile caused by the ablation of Na and K (Janches et al., 2009). These alkali peaks occur at altitudes of 92, 102 and 112 km for entry velocities of 15, 30 and  $60 \text{ km s}^{-1}$ , respectively. For a particle at  $15 \text{ km s}^{-1}$ , organic pyrolysis should produce a distinct detached layer around 100 km, with a peak S/N of  $-7 \text{ dB}$ , significantly above the  $-20 \text{ dB}$  detection limit for the Arecibo radar. For a particle at  $60 \text{ km s}^{-1}$ , the meteor should be observable up to 135 km, 13 km higher than due to ablation/sputtering of the silicate component. We therefore conclude that organic pyrolysis should be observable by a HPLA radar. In fact, organic pyrolysis might explain the discrepancy between the observed height distributions of meteor head echoes made by three HPLA radars, and the modeled distributions assuming only metal silicate ablation, where a significant population of higher altitude meteors were observed than were predicted (Figure 10 in Swarnalingam et al. [2019]). Finally, if organic pyrolysis leads to fragmentation before the dust particle melts, and the resulting silicate subunits are too small to continue heating to above their melting point, this might be observable as a high altitude trail which suddenly terminated.

#### 4.3. How Extensive Is Fragmentation of Cosmic Dust Particles?

To begin to answer this question, consider the organic fraction that would remain for particles of different masses and entry velocities. Figure 8 illustrates the percentage of organic carbon remaining in a particle as a function of entry velocity (at a zenith entry angle of 35°). The results are shown for 5 masses ranging from  $2 \times 10^{-5}$  to  $0.2 \mu\text{g}$ . For each mass, the solid line shows the organic fraction remaining if the particle does not reach the melting point (1800 K) during entry. The end of each solid line therefore indicates the highest velocity a particle of that mass could have to avoid melting. For each mass, the fraction of remaining carbon decreases with increasing entry velocity, because the particle reaches a higher temperature and the pyrolysis rate increases exponentially. The smaller the particle mass/size, the smaller the fraction of carbon lost at a fixed entry velocity. The particles that lose most carbon ( $\sim 98\%$ ) have a mass around  $0.02 \mu\text{g}$  and entry velocity around  $18 \text{ km s}^{-1}$ , because this combination maximizes the flight time where the temperature is above 800 K but does not reach the melting point.

One point to note in Figure 8 is that all the particles we consider here are predicted to lose some organic C, even when entering at the lowest velocity: the smallest particles ( $2 \times 10^{-5} \text{ g}$ ,  $r = 1.3 \mu\text{m}$ ) lose 10% of their organic C, increasing to 75% for the largest particles ( $0.2 \mu\text{g}$ ,  $27.9 \mu\text{m}$ ). This needs to be kept in mind when analyzing IDPs collected in the stratosphere (Flynn et al., 2013; Carrillo-Sánchez et al., 2020a).

The dashed lines in Figure 8 show the organic fraction present at the melting point if the particle heats to above 1800 K. This fraction increases to around 60% at the highest entry velocity, and illustrates the trade-off of the increased rate of particle heating and carbon pyrolysis, against the shorter flight time between the onset of pyrolysis and melting.

The tensile strength measurements made using the AFM show that the meteoritic particles do not become more fragile following organic pyrolysis. As pointed out in Section 3.2, the pressure stress of  $<400 \text{ Pa}$  they would experience during atmospheric entry (Brooke et al., 2017) is at least three orders of magnitude smaller than the measured tensile strength of the heated meteoritic particles. Particles of asteroidal origin, which are more dense than cometary particles (Consolmagno et al., 2008) and therefore more similar to the meteoritic particles used in this study, should therefore rarely fragment during entry.

However, it is possible that more fragile cometary particles fragment. Fresh cometary dust particles collected using the COSIMA instrument on the ROSETTA spacecraft were found to have a tensile strength between  $\sim 0.8$  and  $14 \text{ kPa}$  (Hornung et al., 2016). The lower end of this range is reasonably close to the maximum pressure of  $0.4 \text{ kPa}$  that would be encountered by particles ( $r < 200 \mu\text{m}$ ) at entry velocities up to  $72 \text{ km s}^{-1}$  (Brooke et al., 2017). As shown in Figure 8, a particle larger than  $\sim 5 \mu\text{m}$  (mass  $>10^{-3} \mu\text{g}$ ) can lose more than 80% of its organic component in a narrow velocity window below  $30 \text{ km s}^{-1}$  (e.g., for the  $0.02 \mu\text{g}$  particle, the window is

between 16 and 18 km s<sup>-1</sup>). If this particle was a porous agglomerate with low tensile strength such as observed at comet 67/P (Hornung et al., 2016; Mannel et al., 2019) it might then fragment. The majority of low velocity cometary particles originate from Jupiter-family comets, which have a velocity distribution that strongly peaks below 30 km s<sup>-1</sup> (Carrillo-Sánchez, Gómez-Martín, et al., 2020).

In contrast, particles from Halley Type and Oort cloud comets have broad velocity distributions which peak above 40 km s<sup>-1</sup>. As shown in Figure 8, at these relatively high velocities only 40%–50% of the organic component would be lost before the particle melted. Hence these particles would be much more likely to avoid fragmentation and undergo ablation of their silicate component, producing the metal atoms that are required to explain the vertical fluxes of Na and Fe atoms in the upper mesosphere (Carrillo-Sánchez, Gómez-Martín, et al., 2020).

It therefore seems likely that fragmentation only occurs in a subset of Jupiter Family Cometary particles, where the particle is both a low density agglomerate and has a velocity in a narrow window. If this were not the case, it would be difficult to account for the unaltered IDPs collected in the stratosphere (Flynn et al., 2004; Flynn et al., 2013). Even more challenging would be to explain the flux of IDPs retrieved from the snowpack at Concordia in Antarctica (Rojas et al., 2021), particularly since we have shown that around 94% of these unmelted micrometeorites were likely to have originated from Jupiter-family comets (Carrillo-Sánchez, Gómez-Martín, et al., 2020).

## 5. Summary and Conclusions

In this study we have measured the temperature-dependent pyrolysis rates of organic carbon in micron-sized meteoritic particles. The rates of CO<sub>2</sub> production from a CM2 and CV3 carbonaceous chondrite are shown to be very similar and not dependent on particle size (between 36 and 100 μm). Furthermore, the oxygen required for the conversion of organic C into CO<sub>2</sub> appears to be internal to the particle, so that the pyrolysis rates are independent of the O<sub>2</sub> fugacity up to pressures well above the levels that would be encountered during atmospheric entry. The time-resolved production of CO<sub>2</sub> is consistent with pyrolysis of two organic components, which probably correspond to a relatively volatile soluble organic fraction and a refractory insoluble fraction. A kinetic model was developed to fit the experimental time-resolved profiles, and the resulting rate coefficients imported into the chemical ablation model (CABMOD). This model simulates the contribution of CO<sub>2</sub> and SO<sub>2</sub> produced by organic pyrolysis to the electron production rate along a meteor trail, and demonstrates that organic pyrolysis, which occurs before the ablation of the metallic constituents in the particle, should be detectable using a high performance/large aperture radar. Lastly, CABMOD was used to predict the fraction of the organic component in a cosmic dust particle that would be lost during atmospheric entry. In combination with AFM measurements which show that meteoritic particles become more robust after their organic fragment pyrolyzes, we conclude that dust particles from either the asteroid belt or Halley Type/Oort cloud comets are unlikely to fragment. However, a subset of slow-moving, low density particles from Jupiter-family comets may fragment during entry.

## Data Availability Statement

The data shown in the paper and the SI is available at <http://doi.org/10.5281/zenodo.4776013>. For the purpose of open access, the authors have applied a CC-BY public copyright license to any Author Accepted Manuscript (AAM) version arising from this submission. The authors declare that they have no conflict of interest.

## Acknowledgments

This work was funded by the UK Natural Environment Research Council (Grant No. NE/R011222/1). We thank the British Geological Survey for providing the oil shale sample (Metherhills 1 SSK104938, Core 265200), and Professor Margaret Campbell-Brown (U. Western Ontario) for helpful insights into the potential role of organics in meteor fragmentation.

## References

- Alexander, C. M. O., Cody, G. D., De Gregorio, B. T., Nittler, L. R., & Stroud, R. M. (2017). The nature, origin and modification of insoluble organic matter in chondrites, the major source of Earth's C and N. *Geochemistry*, 77, 227–256. <https://doi.org/10.1016/j.chemer.2017.01.007>
- Ananthakrishna, G., & Krishnamoorthy, S. (2018). A novel approach to modelling nanoindentation instabilities. *Crystals*, 8(5), 200. <https://doi.org/10.3390/cryst8050200>
- Anders, E. (1989). Pre-biotic organic matter from comets and asteroids. *Nature*, 342, 255–257. <https://doi.org/10.1038/342255a0>
- Bajt, S., Sandford, S. A., Flynn, G. J., Matrajt, G., Snead, C. J., Westphal, A. J., & Bradley, J. P. (2009). Infrared spectroscopy of Wild 2 particle hypervelocity tracks in Stardust aerogel: Evidence for the presence of volatile organics in cometary dust. *Meteoritics & Planetary Sciences*, 44, 471–484. <https://doi.org/10.1111/j.1945-5100.2009.tb00745.x>
- Bardyn, A., D. Baklouti, H. Cottin, N. Fray, C. Briosis, J. Paquette, et al. (2017). Carbon-rich dust in comet 67P/Churyumov-Gerasimenko measured by COSIMA/Rosetta, *Monthly Notices of the Royal Astronomical Society*, 469, S712–S722, <https://doi.org/10.1093/mnras/stx2640>

- Bones, D. L., Carrillo-Sanchez, J. D., Kulak, A. N., & Plane, J. M. C. (2019). Ablation of Ni from micrometeoroids in the upper atmosphere: Experimental and computer simulations and implications for Fe ablation. *Planetary and Space Science*, *179*, 104725. <https://doi.org/10.1016/j.pss.2019.104725>
- Bones, D. L., Gómez-Martin, J. C., Empson, C. J., Carrillo-Sánchez, J. D., James, A. D., Conroy, T. P., & Plane, J. M. C. (2016). A novel instrument to measure differential ablation of meteorite samples and proxies: The Meteoric Ablation Simulator (MASI). *Review of Scientific Instruments*, *87*, 094504. <https://doi.org/10.1063/1.4962751>
- Brooke, J. S. A., Feng, W. H., Carrillo-Sanchez, J. D., Mann, G. W., James, A. D., Bardeen, C. G., & Plane, J. M. C. (2017). Meteoric smoke deposition in the polar regions: A comparison of measurements with global atmospheric models. *Journal of Geophysical Research: Atmospheres*, *122*, 11112–11130. <https://doi.org/10.1002/2017jd027143>
- Bufford, D., Liu, Y., Wang, J., Wang, H., & Zhang, X. (2014). In situ nanoindentation study on plasticity and work hardening in aluminium with incoherent twin boundaries. *Nature Communications*, *5*, 5546. <https://doi.org/10.1038/ncomms6546>
- Campbell-Brown, M. D. (2019). Meteoroid structure and fragmentation. *Planetary and Space Science*, *169*, 1–7. <https://doi.org/10.1016/j.pss.2019.03.005>
- Carrillo-Sánchez, J. D., Bones, D. L., Douglas, K. M., Flynn, G. J., Wirick, S., Fegley, B., et al. (2020). Injection of meteoric phosphorus into planetary atmospheres. *Planetary and Space Science*, *187*, 104926. <https://doi.org/10.1016/j.pss.2020.104926>
- Carrillo-Sánchez, J. D., Gómez-Martín, J. C., Bones, D. L., Nesvorný, D., Pokorný, P., Benna, M., et al. (2020b). Cosmic dust fluxes in the atmospheres of Earth, Mars, and Venus. *Icarus*, *335*, 113395. <https://doi.org/10.1016/j.icarus.2019.113395>
- Carrillo-Sánchez, J. D., Nesvorný, D., Pokorný, P., Janches, D., & Plane, J. M. C. (2016). Sources of cosmic dust in the Earth's atmosphere. *Geophysical Research Letters*, *43*, 11979–11986. <https://doi.org/10.1002/2016gl071697>
- Clemett, S. J., Sandford, S. A., Nakamura-Messenger, K., Horz, F., & McKay, D. S. (2010). Complex aromatic hydrocarbons in Stardust samples collected from comet 81P/Wild 2. *Meteoritics & Planetary Sciences*, *45*, 701–722. <https://doi.org/10.1111/j.1945-5100.2010.01062.x>
- Cody, G. D., Heying, E., Alexander, C. M. O., Nittler, L. R., Kilcoyne, A. L. D., Sandford, S. A., & Stroud, R. M. (2011). Establishing a molecular relationship between chondritic and cometary organic solids. *Proceedings of the National Academy of Sciences*, *108*, 19171–19176. <https://doi.org/10.1073/pnas.1015913108>
- Consolmagno, G. J., Britt, D. T., & Macke, R. J. (2008). The significance of meteorite density and porosity. *Chemie Der Erde-Geochemistry*, *68*, 1–29. <https://doi.org/10.1016/j.chemer.2008.01.003>
- Cordier, C., van Ginneken, M., & Folco, L. (2011). Nickel abundance in stony cosmic spherules: Constraining precursor material and formation mechanisms. *Meteoritics & Planetary Sciences*, *46*, 1110–1132. <https://doi.org/10.1111/j.1945-5100.2011.01218.x>
- Court, R. W., & Sephton, M. A. (2009a). Investigating the contribution of methane produced by ablating micrometeorites to the atmosphere of Mars. *Earth and Planetary Science Letters*, *288*, 382–385. <https://doi.org/10.1016/j.epsl.2009.09.041>
- Court, R. W., & Sephton, M. A. (2009b). Meteorite ablation products and their contribution to the atmospheres of terrestrial planets: An experimental study using pyrolysis-FTIR. *Geochimica et Cosmochimica Acta*, *73*, 3512–3521. <https://doi.org/10.1016/j.gca.2009.03.006>
- Court, R. W., & Sephton, M. A. (2011). The contribution of sulphur dioxide from ablating micrometeorites to the atmospheres of Earth and Mars. *Geochimica et Cosmochimica Acta*, *75*, 1704–1717. <https://doi.org/10.1016/j.gca.2011.01.029>
- Court, R. W., & Sephton, M. A. (2014). New estimates of the production of volatile gases from ablating carbonaceous micrometeoroids at Earth and Mars during an E-belt-type Late Heavy Bombardment. *Geochimica et Cosmochimica Acta*, *145*, 175–205. <https://doi.org/10.1016/j.gca.2014.09.010>
- Court, R. W., & Tan, J. (2016). Insights into secondary reactions occurring during atmospheric ablation of micrometeoroids. *Meteoritics & Planetary Sciences*, *51*, 1163–1183. <https://doi.org/10.1111/maps.12652>
- Curtius, J., Weigel, R., Vossing, H. J., Wernli, H., Werner, A., Volk, C. M., et al. (2005). Observations of meteoric material and implications for aerosol nucleation in the winter Arctic lower stratosphere derived from in situ particle measurements. *Atmospheric Chemistry and Physics*, *5*, 3053–3069. <https://doi.org/10.5194/acp-5-3053-2005>
- Cziczko, D. J., Thomson, D. S., & Murphy, D. M. (2001). Ablation, flux, and atmospheric implications of meteors inferred from stratospheric aerosol. *Science*, *291*, 1772–1775. <https://doi.org/10.1126/science.1057737>
- De Leuw, S., Rubin, A. E., & Wasson, J. T. (2010). Carbonates in CM chondrites: Complex formational histories and comparison to carbonates in CI chondrites. *Meteoritics & Planetary Sciences*, *45*, 513–530. <https://doi.org/10.1111/j.1945-5100.2010.01037.x>
- Ebert, M., Weigel, R., Kandler, K., Gunther, G., Molleker, S., Grooss, J. U., et al. (2016). Chemical analysis of refractory stratospheric aerosol particles collected within the arctic vortex and inside polar stratospheric clouds. *Atmospheric Chemistry and Physics*, *16*, 8405–8421. <https://doi.org/10.5194/acp-16-8405-2016>
- Elford, W. G. (2004). Radar observations of meteor trails, and their interpretation using Fresnel holography: A new tool in meteor science. *Atmospheric Chemistry and Physics*, *4*, 911–921. <https://doi.org/10.5194/acp-4-911-2004>
- Flynn, G. J., Keller, L. P., Jacobsen, C., Wirick, S., & Navarro-Gonzalez, R. (2004). An assessment of the amount and types of organic matter contributed to the Earth by interplanetary dust. In M. P. Bernstein, & M. Kress (Eds.), *Space life sciences: Steps toward origin(s) of life* (pp. 57–66). <https://doi.org/10.1016/j.asr.2003.09.036>
- Flynn, G. J., Wirick, S., & Keller, L. P. (2013). Organic grain coatings in primitive interplanetary dust particles: Implications for grain sticking in the Solar Nebula. *Earth Planets and Space*, *65*, 1159–1166. <https://doi.org/10.5047/eps.2013.05.007>
- Friend, P., Hezel, D. C., Barrat, J. A., Zipfel, J., Palme, H., & Metzler, K. (2018). Composition, petrology, and chondrule-matrix complementarity of the recently discovered Jbilet Winselwan CM2 chondrite. *Meteoritics & Planetary Sciences*, *53*, 2470–2491. <https://doi.org/10.1111/maps.13139>
- Genge, M. J., & Grady, M. M. (1998). Melted micrometeorites from Antarctic ice with evidence for the separation of immiscible Fe-Ni-S liquids during entry heating. *Meteoritics & Planetary Sciences*, *33*, 425–434. <https://doi.org/10.1111/j.1945-5100.1998.tb01647.x>
- Gómez-Martín, J. C., Bones, D. L., Carrillo-Sánchez, J. D., James, A. D., Trigo-Rodríguez, J. M., Fegley, B., & Plane, J. M. C. (2017). Novel experimental simulations of the atmospheric injection of meteoric metals. *The Astrophysical Journal*, *836*, 212. <https://doi.org/10.3847/1538-4357/aa5c8f>
- Grady, M. M., Abernethy, F. A. J., Verchovsky, A. B., King, A. J., Schofield, P. F., & Russell, S. S. (2014). The Jbilet Winselwan carbonaceous chondrite 2. Light element geochemistry: Strengthening the link between CM and CO meteorites? *Meteoritics & Planetary Sciences*, *49*, A141. <https://doi.org/10.1111/maps.12359>
- Greshake, A., Klock, W., Arndt, P., Maetz, M., Flynn, G. J., Bajt, S., & Bischoff, A. (1998). Heating experiments simulating atmospheric entry heating of micrometeorites: Clues to their parent body sources. *Meteoritics & Planetary Sciences*, *33*, 267–290. <https://doi.org/10.1111/j.1945-5100.1998.tb01632.x>
- Han, Q., Qu, Z., & Ye, Z. Y. (2018). Research on the mechanical behaviour of shale based on multiscale analysis. *Royal Society Open Science*, *5*, 181039. <https://doi.org/10.1098/rsos.181039>

- Hayatsu, R., Matsuoaka, S., Scott, R. G., Studier, M. H., & Anders, E. (1977). Origin of organic matter in early solar system: 7. Organic polymer in carbonaceous chondrites. *Geochimica et Cosmochimica Acta*, *41*, 1325–1339. [https://doi.org/10.1016/0016-7037\(77\)90076-x](https://doi.org/10.1016/0016-7037(77)90076-x)
- Hayes, J. M. (1967). Organic constituents of meteorites - A review. *Geochimica et Cosmochimica Acta*, *31*, 1395–1440. [https://doi.org/10.1016/0016-7037\(67\)90019-1](https://doi.org/10.1016/0016-7037(67)90019-1)
- Hornung, K., Merouane, S., Hilchenbach, M., Langevin, Y., Mellado, E. M., Della Corte, V., et al. (2016). A first assessment of the strength of cometary particles collected in situ by the COSIMA instrument onboard ROSETTA. *Planetary and Space Science*, *133*, 63–75. <https://doi.org/10.1016/j.pss.2016.07.003>
- Hoyle, C. R., Engel, I., Luo, B. P., Pitts, M. C., Poole, L. R., Grooß, J. U., & Peter, T. (2013). Heterogeneous formation of polar stratospheric clouds—Part 1: Nucleation of nitric acid trihydrate (NAT). *Atmospheric Chemistry and Physics*, *13*, 9577–9595. <https://doi.org/10.5194/acp-13-9577-2013>
- Isnard, R., Bardyn, A., Fray, N., Briois, C., Cottin, H., Paquette, J., et al. (2019). H/C elemental ratio of the refractory organic matter in cometary particles of 67P/Churyumov-Gerasimenko. *Astronomy & Astrophysics*, *630*, A27. <https://doi.org/10.1051/0004-6361/201834797>
- James, A. D., Brooke, J. S. A., Mangan, T. P., Whale, T. F., Plane, J. M. C., & Murray, B. J. (2018). Nucleation of nitric acid hydrates in polar stratospheric clouds by meteoric material. *Atmospheric Chemistry and Physics*, *18*, 4519–4531. <https://doi.org/10.5194/acp-18-4519-2018>
- Janches, D., Dyrud, L. P., Broadley, S. L., & Plane, J. M. C. (2009). First observation of micrometeoroid differential ablation in the atmosphere. *Geophysical Research Letters*, *36*, L06101. <https://doi.org/10.1029/2009gl037389>
- Janches, D., Plane, J. M. C., Nesvorniy, D., Feng, W., Vokrouhlicky, D., & Nicolls, M. J. (2014). Radar detectability studies of slow and small zodiacal dust cloud particles. I. The case of the Arecibo 430 MHz meteor heard echo observations. *The Astrophysical Journal*, *796*, 41. <https://doi.org/10.1088/0004-637x/796/1/41>
- Janches, D., Swarnalingam, N., Carrillo-Sanchez, J. D., Gomez-Martin, J. C., Marshall, R., Nesvorniy, D., et al. (2017). Radar detectability studies of slow and small zodiacal dust cloud particles. III. The role of sodium and the head echo size on the probability of detection. *The Astrophysical Journal*, *843*, 1. <https://doi.org/10.3847/1538-4357/aa775c>
- Jarosewich, E. (1990). Chemical-analyses of meteorites: A compilation of stony and iron meteorite analyses. *Meteoritics*, *25*, 323–337. <https://doi.org/10.1111/j.1945-5100.1990.tb00717.x>
- Jessberger, E. K., Christoforidis, A., & Kissel, J. (1988). Aspects of the major element composition of Halley's dust. *Nature*, *332*, 691–695. <https://doi.org/10.1038/332691a0>
- Jones, W. (1997). Theoretical and observational determinations of the ionization coefficient of meteors. *Monthly Notices of the Royal Astronomical Society*, *288*, 995–1003. <https://doi.org/10.1093/mnras/288.4.995>
- Kar, T., & Hascakir, B. (2017). In situ kerogen extraction via combustion and pyrolysis. *Journal of Petroleum Science and Engineering*, *154*, 502–512. <https://doi.org/10.1016/j.petrol.2017.01.051>
- Kerridge, J. F. (1983). Isotopic composition of carbonaceous-chondrite kerogen—Evidence for an interstellar origin of organic-matter in meteorites. *Earth and Planetary Science Letters*, *64*, 186–200. [https://doi.org/10.1016/0012-821x\(83\)90203-0](https://doi.org/10.1016/0012-821x(83)90203-0)
- Kimura, H., Hilchenbach, M., Merouane, S., Paquette, J., & Stenzel, O. (2020). *The Morphological, Elastic, and Electric Properties of Dust Aggregates in Comets: A Close Look at COSIMA/Rosetta's Data on Dust in Comet 67P/Churyumov-Gerasimenko*, Planet (Vol. 181). Space Science, 104825. <https://doi.org/10.1016/j.pss.2019.104825>
- King, A. J., Russell, S. S., Schofield, P. F., Humphreys-Williams, E. R., Strekopytov, S., et al. (2019). The alteration history of the Jbilet Winselwan CM carbonaceous chondrite: An analog for C-type asteroid sample return. *Meteoritics & Planetary Sciences*, *54*, 521–543. <https://doi.org/10.1111/maps.13224>
- Kissel, J., & Krueger, F. R. (1987). The organic-component in dust from comet Halley as measured by the PUMA mass-spectrometer on board Vega-1. *Nature*, *326*, 755–760. <https://doi.org/10.1038/326755a0>
- Langevin, Y., Hilchenbach, M., Ligier, N., Merouane, S., Hornung, K., Engrand, C., et al. (2016). Typology of dust particles collected by the COSIMA mass spectrometer in the inner coma of 67P/Churyumov Gerasimenko. *Icarus*, *271*, 76–97. <https://doi.org/10.1016/j.icarus.2016.01.027>
- Lowe, D., & MacKenzie, A. R. (2008). Polar stratospheric cloud microphysics and chemistry. *Journal of Atmospheric and Solar-Terrestrial Physics*, *70*, 13–40. <https://doi.org/10.1016/j.jastp.2007.09.011>
- Mannel, T., Bentley, M. S., Boakes, P. D., Jeszenszky, H., Ehrenfreund, P., Engrand, C., et al. (2019). Dust of comet 67P/Churyumov-Gerasimenko collected by Rosetta/MIDAS: Classification and extension to the nanometer scale. *Astronomy & Astrophysics*, *630*, A26. <https://doi.org/10.1051/0004-6361/201834851>
- Morse, A. D., & Chan, Q. H. S. (2019). Observations of cometary organics: A post Rosetta review. *ACS Earth Space Chem*, *3*, 1773–1791. <https://doi.org/10.1021/acsearthspacechem.9b00129>
- Murae, T. (1997). Structure of high-molecular carbonaceous compound in carbonaceous chondrites and formation of IR-spectroscopically similar compounds in the laboratory. In F. Raulin, & J. M. Greenberg (Eds.), *Life sciences: Complex organics in Space* (pp. 1053–1057). [https://doi.org/10.1016/s0273-1177\(97\)00352-9](https://doi.org/10.1016/s0273-1177(97)00352-9)
- Murphy, D. M., Froyd, K. D., Schwarz, J. P., & Wilson, J. C. (2014). Observations of the chemical composition of stratospheric aerosol particles. *Quarterly Journal of the Royal Meteorological Society*, *140*, 1269–1278. <https://doi.org/10.1002/qj.2213>
- Murphy, D. M., Thomson, D. S., & Mahoney, T. M. J. (1998). In situ measurements of organics, meteoritic material, Mercury, and other elements in aerosols at 5 to 19 kilometers. *Science*, *282*, 1664–1669. <https://doi.org/10.1126/science.282.5394.1664>
- NIST Mass Spectrometry Data Center. (2020). Mass spectra. In Linstrom, P. J., & W. G. Mallard (Eds.), *NIST chemistry WebBook, NIST standard reference database number 69*. National Institute of Standards and Technology.20899. <https://doi.org/10.18434/T4D303>
- Nozaki, W., Nakamura, T., & Noguchi, T. (2006). Bulk mineralogical changes of hydrous micrometeorites during heating in the upper atmosphere at temperatures below 1000°C. *Meteoritics & Planetary Sciences*, *41*, 1095–1114. <https://doi.org/10.1111/j.1945-5100.2006.tb00507.x>
- Ozawa, T. (1965). A new method of analyzing thermogravimetric data. *Bulletin of the Chemical Society of Japan*, *38*, 1881–1886. <https://doi.org/10.1246/bcsj.38.1881>
- Plane, J. M. C. (2012). Cosmic dust in the Earth's atmosphere. *Chemical Society Reviews*, *41*, 6507–6518. <https://doi.org/10.1039/c2cs35132c>
- Plane, J. M. C., Feng, W., & Dawkins, E. C. M. (2015). The mesosphere and metals: Chemistry and changes. *Chemical Reviews*, *115*, 4497–4541. <https://doi.org/10.1021/cr500501m>
- Plane, J. M. C., Flynn, G. J., Määttänen, A., Moores, J. E., Poppe, A. R., Carrillo-Sanchez, J. D., & Listowski, C. (2017). Impacts of cosmic dust on planetary atmospheres and surfaces. *Space Science Reviews*, *214*, 23. <https://doi.org/10.1007/s11214-017-0458-1>
- Reddy, K. C., & Premkumar, B. (2019). Meteor head and terminal flare echoes observed with the Gadanki MST radar. *Journal of Atmospheric and Solar-Terrestrial Physics*, *192*, 104952. <https://doi.org/10.1016/j.jastp.2018.11.006>

- Riebe, M. E. I., Foustoukos, D. I., Alexander, C. M. O., Steele, A., Cody, G. D., Mysen, B. O., & Nittler, L. R. (2020). The effects of atmospheric entry heating on organic matter in interplanetary dust particles and micrometeorites. *Earth and Planetary Science Letters*, *540*, 116266. <https://doi.org/10.1016/j.epsl.2020.116266>
- Rietmeijer, F. J. M. (2009). A cometary aggregate interplanetary dust particle as an analog for comet Wild 2 grain chemistry preserved in silica-rich stardust glass. *Meteoritics & Planetary Sciences*, *44*, 1589–1609. <https://doi.org/10.1111/j.1945-5100.2009.tb01193.x>
- Rojas, J., Duprat, J., Engrand, C., Dartois, E., Delauche, L., Godard, M., et al. (2021). The micrometeorite flux at Dome C (Antarctica), monitoring the accretion of extraterrestrial dust on Earth. *Earth and Planetary Science Letters*, *560*, 116794. <https://doi.org/10.1016/j.epsl.2021.116794>
- Ruzicka, A., Grossman, J., Bouvier, A., Herd, C. D. K., & Agee, C. B. (2015). The meteoritical bulletin, No. 102. *Meteoritics & Planetary Sciences*, *50*, 1662. <https://doi.org/10.1111/maps.12491>
- Saleh, R., Robinson, E. S., Ahern, A. T., & Donahue, N. M. (2017). Evaporation rate of particles in the vaporizer of the Aerodyne aerosol mass spectrometer. *Aerosol Science & Technology*, *51*, 501–508. <https://doi.org/10.1080/02786826.2016.1271109>
- Schmitt-Kopplin, P., Gabelica, Z., Gougeon, R. D., Fekete, A., Kanawati, B., Harir, M., et al. (2010). High molecular diversity of extraterrestrial organic matter in Murchison meteorite revealed 40 years after its fall. *Proceedings of the National Academy of Sciences of the United States of America*, *107*, 2763–2768. <https://doi.org/10.1073/pnas.0912157107>
- Schneider, J., Weigel, R., Klimach, T., Dragonas, A., Appel, O., Hunig, A., et al. (2021). Aircraft-based observation of meteoric material in lower-stratospheric aerosol particles between 15 and 68 degrees N. *Atmospheric Chemistry and Physics*, *21*, 989–1013. <https://doi.org/10.5194/acp-21-989-2021>
- Schramm, L. S., Brownlee, D. E., & Wheelock, M. M. (1989). Major element composition of stratospheric micrometeorites. *Meteoritics*, *24*, 99–112. <https://doi.org/10.1111/j.1945-5100.1989.tb00950.x>
- Schuhmann, M., Altwegg, K., Balsiger, H., Berthelier, J. J., De Keyser, J., Fiethe, B., et al. (2019). Aliphatic and aromatic hydrocarbons in comet 67P/Churyumov-Gerasimenko seen by ROSINA. *Astronomy & Astrophysics*, *630*, A31. <https://doi.org/10.1051/0004-6361/201834666>
- Solomon, S. (1999). Stratospheric ozone depletion: A review of concepts and history. *Review of Geophysics*, *37*, 275–316. <https://doi.org/10.1029/1999rg900008>
- Su, X., Chen, P., & Ma, T. (2019). Evaluation of shale fracture toughness based on micrometer indentation test. *Petroleum*, *5*, 52–57. <https://doi.org/10.1016/j.petlm.2018.05.005>
- Swarnalingam, N., Janches, D., Carrillo-Sanchez, J. D., Pokorny, P., Plane, J. M. C., Sternovsky, Z., & Nesvorny, D. (2019). Modeling the altitude distribution of meteor head echoes observed with HPLA radars: Implications for the radar detectability of meteoroid populations. *The Astronomical Journal*, *157*. <https://doi.org/10.3847/1538-3881/ab0ec6>
- Thomas, E., Horanyi, M., Janches, D., Munsat, T., Simolka, J., & Sternovsky, Z. (2016). Measurements of the ionization coefficient of simulated iron micrometeoroids. *Geophysical Research Letters*, *43*, 3645–3652. <https://doi.org/10.1002/2016gl068854>
- Thomas, K. L., Keller, L. P., Blanford, G. E., & McKay, D. S. (1994). Quantitative-analyses of carbon in anhydrous and hydrated interplanetary dust particles. In M. E. Zolensky, T. L. Wilson, F. J. M. Rietmeijer, & G. J. Flynn (Eds.), *Analysis of interplanetary dust* (pp. 165–172). American Institute of Physics. <https://doi.org/10.1063/1.46532>
- Thompson, M. A., Telus, M., Schaefer, L., Fortney, J. J., Joshi, T., & Lederman, D. (2021). Composition of terrestrial exoplanet atmospheres from meteorite outgassing experiments. *Nature Astronomy*, early access. <https://doi.org/10.1038/s41550-021-01338-8>
- Tolbert, M. A., & Toon, O. B. (2001). Atmospheric science—Solving the PSC mystery. *Science*, *292*, 61–63. <https://doi.org/10.1126/science.1060083>
- Toppani, A., Libourel, G., Engrand, C., & Maurette, M. (2001). Experimental simulation of atmospheric entry of micrometeorites. *Meteoritics & Planetary Sciences*, *36*, 1377–1396. <https://doi.org/10.1111/j.1945-5100.2001.tb01831.x>
- Voigt, C., Schlager, H., Luo, B. P., Dornbrack, A. D., Roiger, A., Stock, P., et al. (2005). Nitric acid trihydrate (NAT) formation at low NAT supersaturation in polar stratospheric clouds (PSCs). *Atmospheric Chemistry and Physics*, *5*, 1371–1380. <https://doi.org/10.5194/acp-5-1371-2005>
- Vojacek, V., Borovicka, J., Koten, P., Spurny, P., & Stork, R. (2019). Properties of small meteoroids studied by meteor video observations. *Astronomy & Astrophysics*, *621*, A68. <https://doi.org/10.1051/0004-6361/201833289>
- Vondrak, T., Plane, J. M. C., Broadley, S., & Janches, D. (2008). A chemical model of meteoric ablation. *Atmospheric Chemistry and Physics*, *8*, 7015–7031. <https://doi.org/10.5194/acp-8-7015-2008>
- Vyazovkin, S. (1996). A unified approach to kinetic processing of nonisothermal data. *International Journal of Chemical Kinetics*, *28*, 95–101. [https://doi.org/10.1002/\(sici\)1097-4601\(1996\)28:2<95::aid-kin4>3.0.co;2-g](https://doi.org/10.1002/(sici)1097-4601(1996)28:2<95::aid-kin4>3.0.co;2-g)
- Weigel, R., Volk, C. M., Kandler, K., Hosen, E., Gunther, G., Vogel, B., et al. (2014). Enhancements of the refractory submicron aerosol fraction in the Arctic polar vortex: Feature or exception? *Atmospheric Chemistry and Physics*, *14*, 12319–12342. <https://doi.org/10.5194/acp-14-12319-2014>
- Zhu, Q., Dinsmore, R., Gao, B. Y., & Mathews, J. D. (2016). High-resolution radar observations of meteoroid fragmentation and flaring at the Jicamarca Radio Observatory. *Monthly Notices of the Royal Astronomical Society*, *457*, 1759–1769. <https://doi.org/10.1093/mnras/stw070>